Numerical experiments on scalar transport and mixing in turbulent boundary layers

Journal of Physics: Conference Series **2753** (2024) 012003 doi:10.1088/1742-6596/2753/1/012003

Numerical experiments on scalar transport and mixing in turbulent boundary layers

Gabriele Boga, Alfonso Giancola and Andrea Cimarelli

Dipartimento di Ingegneria Enzo Ferrari, Università di Modena e Reggio Emilia, 41125 Modena, Italy

E-mail: gabriele.boga@unimore.it

Abstract. In this work, we present numerical experiments aimed at dynamically establishing the separate role of the inner and outer cycles on the scalar transport in the configuration of a temporally evolving boundary layer. The experiments are based on the study of the evolution of passive scalars driven by velocity fields where inner and outer cycles are alternately suppressed. Two different approaches are implemented. In the first, the discrimination between inner and outer cycle activities is based on the scale dimension of the involved motions. The second instead, discriminates on the basis of the distance from the wall of the turbulent motions. The two approaches depict the same scenario. Both the inner and outer cycles appear to be autonomous and, in a sense, independent, since their dynamics remain qualitatively unaltered despite facing two different conditions. The outer cycle faces a free boundary at the top and simply rescales according to what is supplied by the inner cycle. The inner cycle, on the other hand, resides between the wall and the outer region. As a result, the reduction of the scalar fluxes in the outer region due to the suppression of the outer cycle causes a damping in the near-wall region activities.

1. Introduction

Wall flows are among the most technologically relevant flows and despite numerous studies (see [1] for a partial review) their dynamic is not yet fully understood. In this family of flows, it is common to identify different regions based on their features. One of the categorisations distinguishes a near-wall region, a bulk region and an overlap region in between. In the near-wall region, the production of turbulent fluctuations exceeds their dissipation rate. The excess is transported towards the wall and towards the bulk region, where is finally dissipated. The overlap region lying between these two layers constitutes a region of local equilibrium between production and dissipation. The near-wall layer is certainly crucial to the dynamics of attached shear flows: it is dominated by intense interacting structures ([2] and [3]) and it is the seat of the highest rate of turbulent energy production and of the maximum turbulent intensities. In this region, turbulence is sustained by a self-sustaining and autonomous cycle [4] which we will refer to as the near-wall cycle. However, for high Reynolds numbers, also the outer overlap layer is thought to become relevant being the site of self-sustaining mechanisms of large flow structures following mixed inner/outer scaling [5]. It is then of overwhelming importance to assess the combined role played by inner and outer turbulence self-sustaining mechanisms in determining the overall momentum and heat transfer in wall turbulence at relatively high Reynolds numbers. In order to identify the separate role of these two layers on mixing and transport that is otherwise

concealed by the non-linearity of the flow evolution, we perform numerical experiments where scalar fields dynamically evolve under the separate action of the sole near-wall cycle and of the sole outer cycle. The choice of addressing the scalar field evolution is crucial to decouple the effect of the two layers. More specifically, we analyse the evolution of passive scalars in the configuration of a temporally evolving boundary layer ([6], [7] and [8]). The flow configuration of the boundary layer is chosen as it represents a canonical flow for the study of wall turbulence and additionally exhibits the presence of a Turbulent/Non-Turbulent Interface (TNTI). For this reason, the boundary layer is also a case study for the turbulent entrainment process ([9] and [10]) that has already been studied with a similar approach in the flow configuration of a temporally evolving planar jet in [11]. The Schmidt number for the scalars is set to $Sc = 1$ in order to rely on the Reynolds analogy linking the scalar and momentum transports. Hence, these experiments aim at dynamically establishing the separate role played by the inner and outer layers in determining the overall transport mechanisms in wall turbulence. The paper is organized as follows. The methodology is covered in section 2, the results are presented and discussed in section 3 and the paper concludes with final remarks in section 4.

2. Simulations and experimental set-up

In the following section we present the methodology used to carry out the experiments, starting with the presentation of the chosen flow configuration, the description of the experimental set-up and a final brief section regarding the filtering operation used in the experiments.

2.1. Temporal boundary layer

The flow selected for the numerical experiments is a temporal boundary layer. This flow has already been investigated through direct numerical simulations and presents all the main phenomena observed in the classical turbulent boundary layer [7]. This type of flow consists in a moving wall at constant speed U_w and scalar concentration Θ_w at the bottom of an initially quiescent fluid. The initial velocity and scalar profiles are designed to mimic the wake of a wall-mounted trip wire with diameter D,

$$u^*(x^*, y^*, z^*, t^* = 0) = \left(1 + c'\right) \frac{U_w}{2} \left[1 + \tanh\left(\frac{D - z^*}{2h}\right)\right] \tag{1}$$

$$\theta^*(x^*, y^*, z^*, t^* = 0) = \frac{\Theta_w}{2} \left[1 + \tanh\left(\frac{D - z^*}{2h_\theta}\right)\right] \tag{2}$$

where $h = 54\nu/U_w$ and $h_\theta = 54\alpha/\Theta_w$ can be understood as the shear-layer thickness of the wall-mounted trip wire and $c'(x^*, y^*, z^*) \in [-0.05, 0.05]$ is a superimposed white noise used to speed up transition. Here, ν is the kinematic viscosity and α is the scalar diffusivity. The Reynolds number based on the tripping thickness is set to $Re_D = U_w D/\nu = 500$ and the Schmidt number is set to $Sc = \nu/\alpha = 1$. In the above initial conditions, the asterisk is used to denote dimensional quantities. In the rest of the paper, equations and quantities, unless otherwise specified, are expressed in dimensionless form by using D, U_w and Θ_w.

The boundary layer develops in time rather than in space (figure 1), preserving statistical homogeneity in the streamwise (x) as well as in the spanwise (y) direction. The advantages of this type of flow over a spatially developing boundary layer are the additional direction of statistical homogeneity and the possibility of using domains of reduced streamwise extension.

Periodic boundary conditions are applied in the streamwise and spanwise directions, while a Dirichlet no-slip boundary condition and a free-slip impermeable boundary condition are applied on the bottom and the top of the domain respectively. The domain extension in the streamwise, spanwise and wall-normal directions is respectively $(Lx, Ly, Lz) = (600, 300, 150)$ discretised in $(Nx, Ny, Nz) = (512, 512, 384)$ points. It is important to note that the domain dimensions are

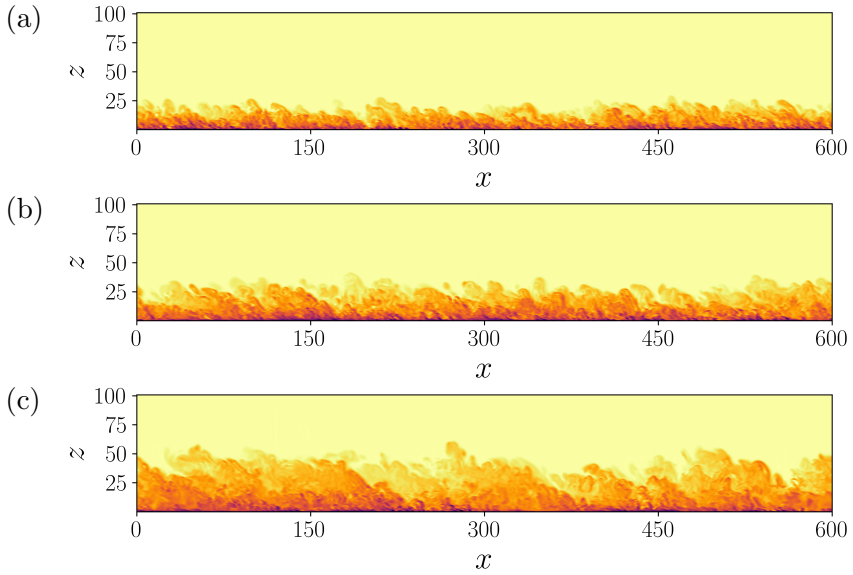

Figure 1. Sections of the scalar field at different time instants corresponding respectively to (a) $Re_\tau = 500$, (b) $Re_\tau = 750$ and (c) $Re_\tau = 1000$. The scalar concentration increases from light to dark colors.

chosen to guarantee that at the final friction Reynolds number the boundary layer thickness is $\delta < L_z/3$ in order to have reasonably small confinement effects from the top boundary. Here, the boundary layer thickness δ is defined such that $\langle u \rangle (\delta) = 0.01 U_w$. The domain dimensions in terms of boundary layer thickness and the grid resolution in terms of friction units are reported in table 1. The final friction Reynolds number reached by the simulations is $Re_\tau = u_\tau \delta/\nu = 1000$, where $u_\tau = \sqrt{\tau_w/\rho}$ is the friction velocity and τ_w and ρ are respectively the wall shear stress and the density.

The set of equations is solved using the massively-parallel open-source code CaNS [12], which uses a pressure-projection method with a second-order finite-difference scheme for the spatial discretization on a staggered grid. A mixed time integration is used to avoid the very small time-step required by the highly stretched grid. For the diffusion terms in the vertical direction z an implicit time integration is used, employing the Crank-Nicholson scheme. Conversely, all the other terms are integrated explicitly in time with a three-step Runge–Kutta method with a $CFL = 0.7$. In this preliminary work, we opted for low resolution simulations to test the

Table 1. Domain extension in terms of boundary layer thickness and grid resolution in friction units for three different time instants corresponding to three different friction Reynolds numbers. The subscript $\cdot_{|w}$ and $\cdot_{|\delta}$ indicates a quantity measured respectively at the wall ($z = 0$) and at $z = \delta$.

Re_τ	$(Lx, Ly, Lz)\,/\delta$	Δx^+	Δy^+	$\Delta z^+_{\|w}$	$\Delta z^+_{\|\delta}$
500	(26.73, 13.36, 6.68)	26.06	13.03	0.14	7.86
750	(16.95, 8.47, 4.24)	24.78	12.39	0.13	10.46
1000	(12.37, 6.18, 3.09)	23.83	11.91	0.13	12.47

potential of the method used. We verified that the classical statistics obtained with these settings are reliable when compared to those obtained from higher resolution simulations presented in [8].

2.2. Numerical experiments

As mentioned above, the inner and outer cycles interact with each other and their combined role governs the exchange of momentum and scalar concentration. Understanding the role played by these two cycles is therefore of great interest, both from a flow control and modelling perspective. In this regard, the present work aims to dynamically establish the role played by these two mechanisms by analysing the evolution of two additional passive scalars transported by two modified velocity fields where the near-wall and outer cycles are alternatively suppressed. The two modified velocity fields are obtained through a filtering operation performed at runtime. It is important to note that the filtering operation is not directly applied to the scalar fields, but it is only used to obtain the two modified velocity fields transporting the two alternative scalars. These velocity fields are not integrated over time but are obtained at each time-step from the total velocity. The resulting set of equations is:

$$\begin{aligned}
&\frac{\partial u_i}{\partial x_i} = 0 \\
&\frac{\partial u_i}{\partial t} + \frac{\partial u_i u_j}{\partial x_j} = -\frac{\partial p}{\partial x_i} + \frac{1}{Re}\frac{\partial^2 u_i}{\partial x_j \partial x_j} \\
&\frac{\partial \theta}{\partial t} + \frac{\partial \theta u_j}{\partial x_j} = \frac{1}{ReSc}\frac{\partial^2 \theta}{\partial x_j \partial x_j} \\
&\frac{\partial \theta}{\partial t} + \frac{\partial \theta u_j}{\partial x_j} = \frac{1}{ReSc}\frac{\partial^2 \theta}{\partial x_j \partial x_j} \\
&\frac{\partial \theta_{out}}{\partial t} + \frac{\partial \theta_{out} u_j^{out}}{\partial x_j} = \frac{1}{ReSc}\frac{\partial^2 \theta_{out}}{\partial x_j \partial x_j} \\
&\frac{\partial \theta_{inn}}{\partial t} + \frac{\partial \theta_{inn} u_j^{inn}}{\partial x_j} = \frac{1}{ReSc}\frac{\partial^2 \theta_{inn}}{\partial x_j \partial x_j}
\end{aligned} \tag{3}$$

where θ is the passive scalar transported by the complete velocity field u_i, θ_{out} is the scalar transported by velocity field retaining the sole outer cycle u_i^{out} and θ_{inn} is the scalar field transported by the velocity field retaining the sole inner cycle u_i^{inn}. The initial condition for the two scalar fields θ_{out} and θ_{inn} is taken from the reference case θ at a time instant corresponding to $Re_\tau = 500$.

2.3. Filtering

Two different filtering approaches have been tested. For the sake of clarity, in the present section we will describe only the first approach, the results of which are presented in section 3, while we leave the description and the results of the second approach in Appendix A. In both approaches, the filter used is a 2D Gaussian filter applied in the homogeneous directions x and y,

$$\overline{u}_i(x,y,z,t) = \int_{-\infty}^{+\infty}\int_{-\infty}^{+\infty} u_i(x+r_x, y+r_y, z, t)\, G(r_x, r_y)\, dr_x dr_y, \tag{4}$$

$$G(r_x, r_y) = \frac{1}{2\pi\Delta_x\Delta_y} e^{-\frac{1}{2}\left(\frac{r_x^2}{\Delta_x^2}+\frac{r_y^2}{\Delta_y^2}\right)} \tag{5}$$

where $\overline{u}_i$ is the resulting filtered velocity and Δ_x and Δ_y are the characteristic lengths of the filter in the streamwise and spanwise directions. In the first approach, the above filtering operation is applied to the whole domain. The velocity field retaining the sole outer cycle is defined as $u_i^{out} = \overline{u}_i$ and, hence, it contains only the large-scale motions, which are those mainly contributing to the outer cycle dynamics. On the other hand, the velocity field retaining the sole inner cycle u_i^{inn} is defined as $u_i^{inn} = u_i - \overline{u}_i + \langle u_i \rangle$, and hence, it contains only the small-scale motions that are dominant in the near-wall cycle, being large-scale motions merely an imprinting from the outer flow. The action of the average velocity $\langle u_i \rangle(z,t)$ (being $\langle \cdot \rangle$ the average operator in the homogeneous directions x and y) is added explicitly, since $\langle u_i - \overline{u}_i \rangle = 0$. The filter lengths are chosen on the basis of the premultiplied spectra shown in figure 2 and are respectively set to $\Delta_x^+ = 600$ and $\Delta_y^+ = 100$. The portions of the spectra filtered out in the spanwise direction to obtain u_i^{inn} and u_i^{out} are shown in shaded grey in figure 2(a) and (b), respectively measured in the buffer layer and in the outer region. Note that the shaded grey areas shown in figure 2 are merely indicative since the Gaussian filter does not prescribe a sharp cut-off scale in spectral space.

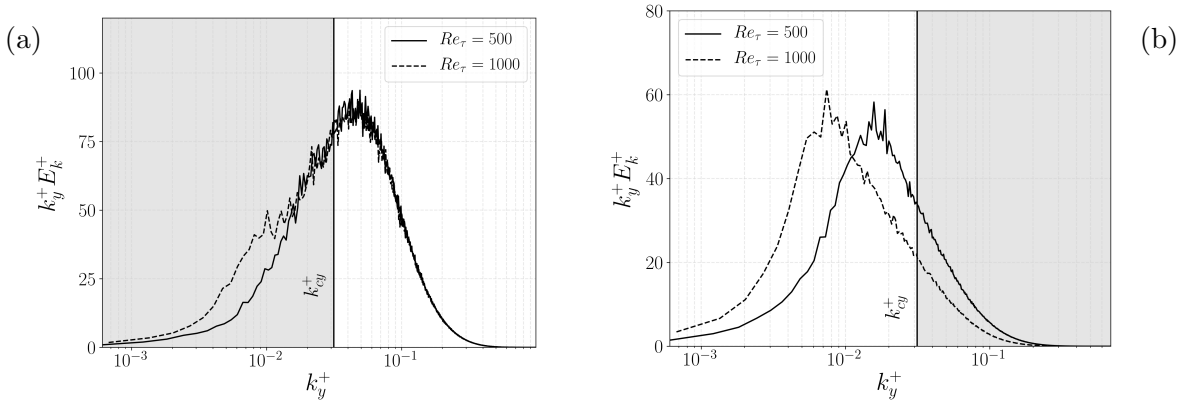

Figure 2. Premultiplied spectra of the turbulent kinetic energy E_k in the spanwise wavenumber k_y respectively (a) in the buffer layer at $z^+ = 20$ and (b) in the outer region at $z = 0.3\delta$. The shaded areas are indicative of the filtered regions of the spectra (a) in u_{inn} and (b) in u_{out}, being $k_{cy}^+ = 2\pi/\Delta_y^+$ the wavenumber corresponding to the spanwise filter length in inner units.

3. Results

Let us start analysing the scalar field topology at the final friction Reynolds number $Re_\tau = 1000$ reached during the experiments. In figure 3 the instantaneous scalar contours are shown on a wall-normal (x, z) section. The trace of the large engulfing scales is clearly visible in θ_{out} and, at first glance, the thickness of the boundary layer seems comparable to that of the reference case θ. Concurrently, the effect of the lack of the small scales can be seen in the presence of large unmixed regions. On the contrary, the field θ_{inn} appears to be more mixed and exhibits a slower growth rate, which can be attributed to the lack of large-scale engulfment events.

We now proceed to analyse the data from a statistical point of view, starting with the temporal evolution of two integral quantities reported in figure 4, the Stanton number

$$St = -\frac{1}{ReSc} \left. \frac{\partial \langle \theta \rangle}{\partial z} \right|_w \tag{6}$$

and the boundary layer thickness based on the scalar concentration δ_θ, defined such that $\langle \theta \rangle(\delta_\theta) = 0.01\Theta_w$. In order to better understand the reason behind the observations, we report

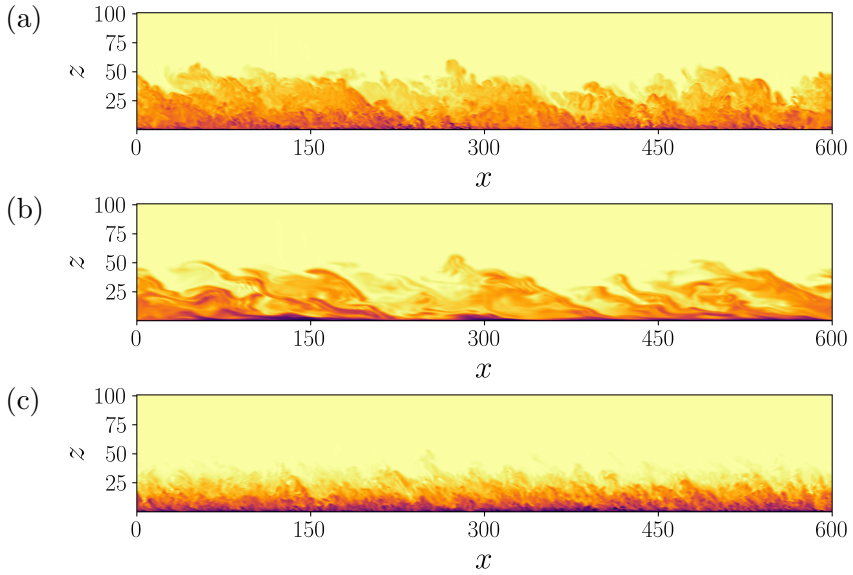

Figure 3. Sections of the scalar fields of the three experiments at the same time instant, corresponding to $Re_\tau = 1000$. Respectively (a) θ, (b) θ_{out} and (c) θ_{inn}. The reference case (a) is duplicated here in order to simplify comparisons.

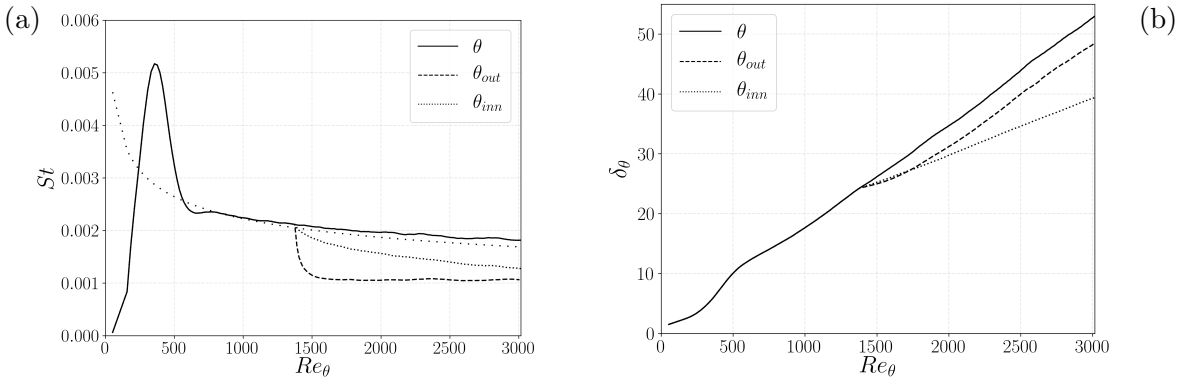

Figure 4. (a) Temporal evolution of the Stanton number and its theoretical law $St = 0.0125 Re_\theta^{-1/4}$ in loosely dotted line ($\cdots\cdots$) and (b) temporal evolution of the boundary layer thickness based on the scalar concentration δ_θ.

the probability density function of the scalar fields at some locations of interest for the observed quantities (i.e. in the viscous sub-layer for St and at the mean scalar interface for δ_θ) in figure 5. A reduction in St can be noticed in both the experiments. The reduction observed in θ_{out} (dashed line in figure 4(a)) can be interpreted as the effect of the direct suppression of the main turbulent motions involved in the near-wall cycle, leading to an almost immediate decrease. This hypothesis is supported by the lower anisotropy observed in the near-wall region fluctuations that can be visualized as the limited extension of the left tail of the θ_{out} pdf reported in figure 5(a). On the other hand, the field θ_{inn} (dotted line) preserves the scales directly contributing to the wall scalar transfer. In this case, the reduction in St can be attributed to the increase in the mean scalar concentration resulting from the suppression of the outer cycle, thus justifying the more gradual decrease with respect to θ_{out}. Support for this can be found in the fact that θ_{inn}

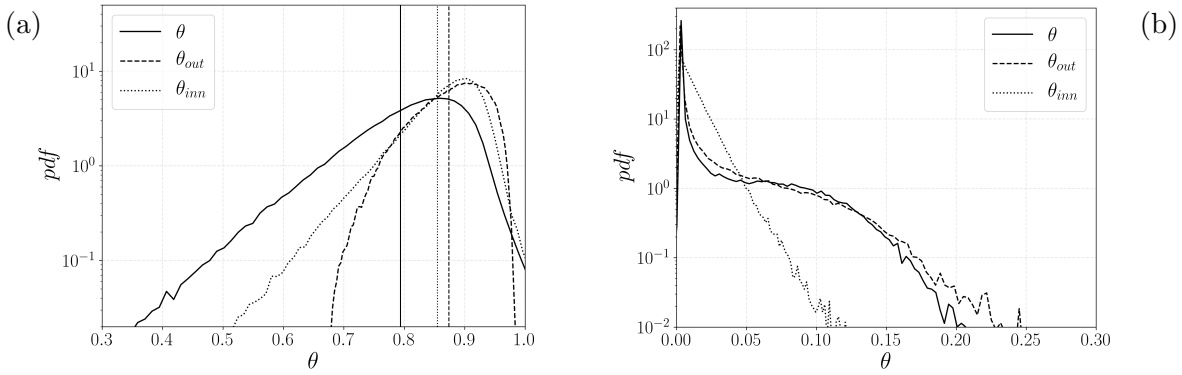

Figure 5. Probability density function of θ (a) at $z^+ = 5$ and (b) at $z = \delta_\theta$ at the final $Re_\tau = 1000$. The vertical lines in (a) indicate the respective mean values of the scalars.

shows a similar pdf to that of θ, the difference being its shift towards higher values (figure 5(a)). We now consider the temporal evolution of the boundary layer thickness δ_θ reported in figure 4(b). After an initial readjustment, the trend of $\delta_{\theta_{out}}$ resumes a growth rate similar to that of the reference δ_θ. This almost unchanged growth rate can be explained through the following two considerations. The first is that large-scale anisotropic motions that mainly contribute to the entrainment process ([11]) are preserved in u_i^{out}, whose trace can be seen in the right tail of the θ_{out} pdf reported in figure 5(b). The second consideration regards the measured observable δ_θ. In fact, the position of the mean interface is not sensitive to the threshold used. For this reason, the reduction in the scalar concentration flux supplied by the inner region in θ_{out} has little influence on the evolution of this observable. On the contrary, the suppression of the large anisotropic motions in u_i^{inn} directly acts on the entrainment process at the interface of the boundary layer, resulting in the slower growth rate of $\delta_{\theta_{inn}}$.

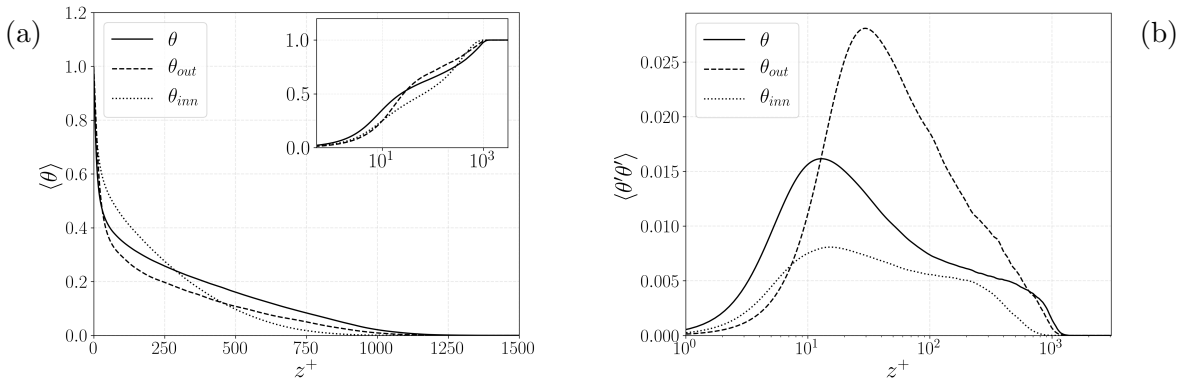

Figure 6. (a) Mean scalar profiles, respectively $\langle\theta\rangle$ in the main panel and $1 - \langle\theta\rangle$ in semi-logarithmic axes in the inset panel and (b) variances at $Re_\tau = 1000$.

For a deeper understanding of the dynamics observed so far, we now move to examine the mean profiles and the variances of the scalar fields reported in figure 6. Both profiles $\langle\theta_{out}\rangle$ and $\langle\theta_{inn}\rangle$ show a higher scalar concentration in the near-wall region, for $z^+ < 20$. This is in accordance with the reduction observed in the St for the two reasons explained above, namely: the reduced scalar flux towards the outer region caused by the suppression of the inner cycle in θ_{out} and the blockage effect caused by the suppression of the outer cycle in θ_{inn} (that will be

shown in figure 7). Despite a different distribution of the scalar concentration $\langle\theta_{out}\rangle$, a region resembling a logarithmic behaviour can still be observed as shown in the inset of figure 6(a). The lower scalar flux supplied by the near-wall region does not seem to influence the outer dynamics of θ_{out}. On the other hand, θ_{inn} presents a qualitatively different profile. The suppression of the outer cycle, with the associated reduction of the mean scalar flux, results in a high scalar concentration region extending from the near-wall up to a good portion of the outer region.

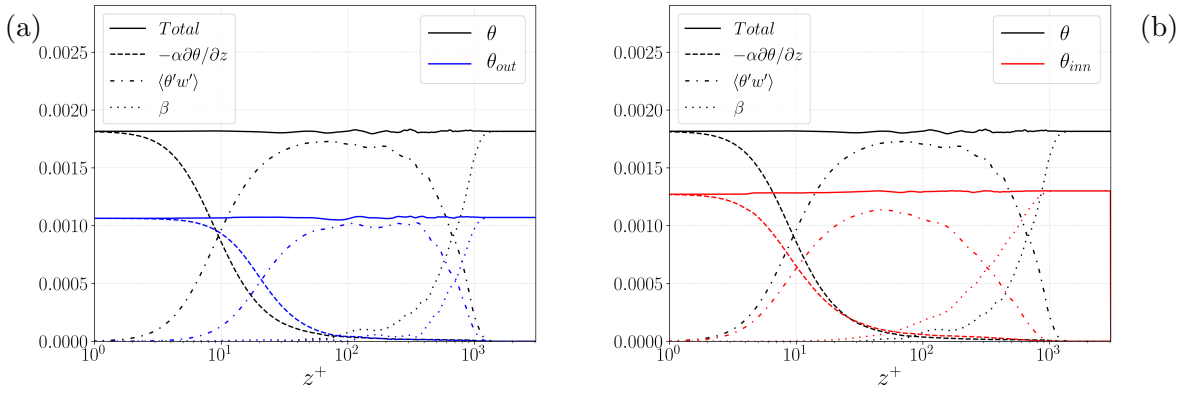

Figure 7. Mean fluxes of (a) θ_{out} and (b) θ_{inn} compared with θ at $Re_\tau = 1000$.

In order to quantify the reduction of the fluxes, we introduce the following equation:

$$St = \langle\theta'w'\rangle - \frac{1}{ReSc}\frac{\partial\langle\theta\rangle}{\partial z} + \beta \quad \text{with} \quad \beta = \frac{d}{dt}\int_0^z \langle\theta\rangle dz \tag{7}$$

obtained by integrating in the wall-normal direction the equation for the mean scalar concentration. To note that, for $z \gg \delta_\theta$ the above equation simply reads $St = \beta\,(z \to \infty)$, where $\beta\,(z \to \infty)$ is the rate of entrainment of scalar concentration. The terms of equation (7) of the two experiments are shown and compared with the reference case in figure 7. At first glance, one can see a macroscopic similarity in the shape of the fluxes with a global reduction in accordance with the reduction observed in the St. Taking a closer look to the turbulent flux, it can be seen that $\langle\theta'_{out}w'_{out}\rangle$ appears to be more active at a higher distance from the wall, while $\langle\theta'_{inn}w'_{inn}\rangle$ appears to be more active closer to the wall, as expected. Since $\langle\theta'w'\rangle$ and β must sum up to St in the outer region (where $-k\partial\theta/\partial z$ is negligible), these different profiles of $\langle\theta'w'\rangle$ determine also the shape of β. The high activity of $\langle\theta'_{out}w'_{out}\rangle$ in the outer region results in a steep profile of β_{out}, meaning that the scalar flux is mainly sustained by the entrainment process occurring away from the wall and near the interface. On the contrary, the lower activity of $\langle\theta'_{inn}w'_{inn}\rangle$ in the outer region results in a less steep profile of β_{inn}, suggesting that the main scalar flux is sustained by the homogenization in the core of the boundary layer, thus by the mixing effect of the small quasi-isotropic scales. Despite the similarity between the mean profiles of θ_{out} and θ, their variances, reported in figure 6(b), present different characteristics. In particular, $\langle\theta'_{out}\theta'_{out}\rangle$ exhibits a more pronounced peak located at a greater distance from the wall with respect to $\langle\theta'\theta'\rangle$. This difference can be attributed to the presence of large unmixed regions initiated by the large-scale anisotropic motions and left unmixed by the absence of the small mixing scales. Conversely, the profile of $\langle\theta'_{inn}\theta'_{inn}\rangle$ resembles the reference profile, although it appears to be damped, indicating a more uniform field. Both $\langle\theta'_{out}\theta'_{out}\rangle$ and $\langle\theta'_{inn}\theta'_{inn}\rangle$ present lower values in the near-wall region with respect to the reference case.

In order to take a closer look into the dynamics of the scalar fluctuations we introduce the scalar variance budget equation:

$$\frac{\partial\langle\theta'\theta'\rangle}{\partial t} + \frac{\partial}{\partial z}\left(\Phi_u + \Phi_\alpha\right) = \Pi - \epsilon_\theta \tag{8}$$

where the turbulent production Π and dissipation ϵ_θ terms are defined as:

$$\Pi = -2\langle\theta' w'\rangle\frac{\partial\langle\theta\rangle}{\partial z} \quad \text{and} \quad \epsilon_\theta = \frac{2}{ReSc}\langle\frac{\partial\theta'}{\partial x_j}\frac{\partial\theta'}{\partial x_j}\rangle \tag{9}$$

and the turbulent Φ_u and diffusive Φ_α fluxes as:

$$\Phi_u = \langle\theta'\theta' w'\rangle \quad \text{and} \quad \Phi_\alpha = \frac{-1}{ReSc}\frac{\partial\langle\theta'\theta'\rangle}{\partial z} \tag{10}$$

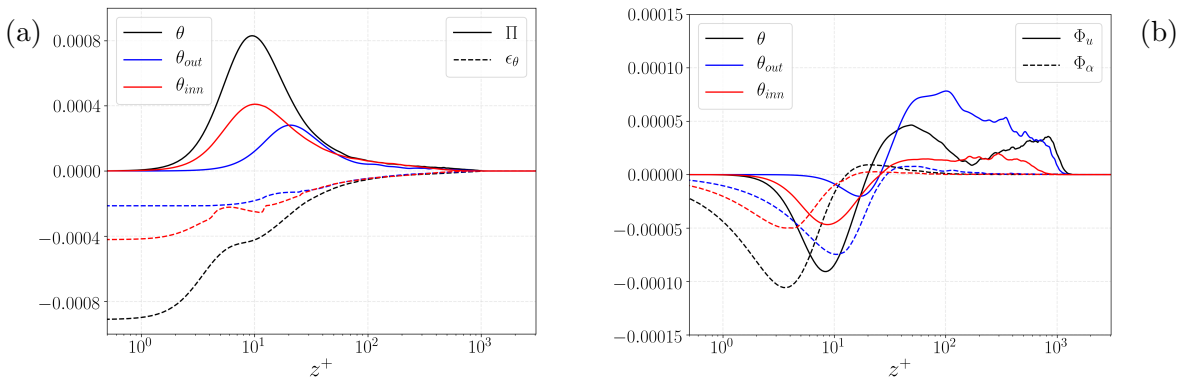

Figure 8. Scalar variance (a) production Π, dissipation ϵ_θ and (b) turbulent and diffusive fluxes Φ_u and Φ_α at $Re_\tau = 1000$.

The picture shown by the scalar variance budget in figure 8 can be interpreted as follows. Both the scalar variance production and the turbulent flux towards the near-wall region are strongly reduced in θ_{out}, thus justifying the lower scalar variance observed in the near-wall region. In addition to this reduction, a shift to higher wall distances can also be observed, reinforcing the idea that large-scale motions are not directly active in the near-wall region, beside the imprinting they give on the flow and the modulation with which they act on the small scales. The diffusive flux and the dissipation adapt themselves to this scenario. On the other hand, the inner dynamics of θ_{inn} appear qualitatively similar to the reference case, even if lower in intensity. This is in accordance with the idea that the inner cycle finds itself in a condition bounded by the outer dynamics but remains qualitatively unaltered. In particular, the suppression of the outer cycle limits the turbulent flux of fluctuations directed toward the wall, and the increase of the mean scalar value limits the possibility of a large variance because of the intrinsic limitation $\theta \leq 1$.

4. Conclusions

An attempt to decouple the dynamics of the inner and outer cycles in the flow configuration of a temporally evolving boundary layer is carried out. The attempt is based on studying the evolution of two additional passive scalars driven by two modified velocity fields. The use of the two scalar fields is the key point that allows us to separate the two effects, as it permits us to study a field on which no direct manipulation has been applied. The velocity fields used to transport these two additional scalars are obtained at each timestep by manipulating the total velocity u_i in order to retain only features of the inner (u_i^{inn}) and outer (u_i^{out}) cycles

respectively. More specifically, the two velocity fields are obtained by suppressing scales that are mostly contributing to the inner or outer cycle activities based on their dimension.

The outer cycle dynamics observed through θ_{out} show many similarities with the reference case θ. In both the approaches tested, it seems possible to identify a logarithmic-like region in the mean profile $\langle\theta_{out}\rangle$. Furthermore, the growth rate of the scalar boundary layer thickness $\delta_{\theta_{out}}$ is unaltered, indicating that the entrainment process at the boundary layer interface is not very sensitive to the near-wall region dynamics. At the same time, in the region directly affected in this experiment (i.e. the inner region), the effect of inner cycle suppression can be observed. In this region, both a reduction in the scalar transfer at the wall (caused by the damping of the scalar fluctuations) and a reduction of turbulent production and transport mechanisms occurs. In particular, the reduction of the mean scalar flux in the near-wall region also implies a reduction in the whole domain due to the conservation law. Summarising, by suppressing the small scales, the outer cycle appears to maintain its dynamics unaltered and simply rescales the scalar flux according to what is supplied by the flux coming from the inner cycle. From a modelling perspective, this conclusion may be relevant for reduced-order approaches such as wall-modelled LES and RANS.

The inner cycle, on the other hand, is confined on both sides, facing the wall at its lower boundary and the outer cycle on the other side. The suppression of the outer cycle appears to have the effect of a bottleneck for the inner cycle. This interpretation is supported by the fact that the pdf of θ_{inn} in the near-wall region shows a similar distribution but with a shift towards higher values (reason for the gradual reduction of the Stanton number). Other symptoms of an almost unchanged dynamic can be found in the production and turbulent transport mechanisms in the near-wall region. Despite appearing rescaled, these profiles show a very similar shape to the reference case θ. In the outer region of θ_{inn}, the suppression of the large anisotropic scales has the effect of reducing the rate of entrainment and the generation of a more homogeneous scalar field.

In conclusion, both the inner and outer cycles appear to have quite independent dynamics, with the difference being that, the outer cycle simply rescales to lower scalar values depending on what is supplied from the inner cycle, facing a free region on its top bound. On the other hand, the inner cycle dynamics is confined to operate in between the wall and the outer cycle, the suppression of which can act as a bound, limiting the inner cycle to operate in a narrower and narrower range of scalar values due to the intrinsic limitation $\theta \leq 1$.

Acknowledgments
This work was performed in part during the Fifth Madrid Turbulence Workshop, funded by the European Research Council under the Caust grant ERCAdG-101018287. The authors would like to thank Prof. Jiménez for organizing the event.

Appendix A. Effect of the filtering procedure

In order to show the robustness of the present results on the type of filtering procedure adopted, we present here the results obtained through a different filtering approach. This second approach tested uses the filtering operation only in sub-portions of the domain to obtain the two modified velocity fields. The field u_i^{out} is obtained by lowpass filtering the near-wall region ($z^+ < 60 = z_c^+$) in order to suppress the inner cycle and leave the outer cycle motions unaltered. On the other hand u_i^{inn} is obtained by lowpass filtering the outer region ($z^+ > 60 = z_c^+$) and leaving the velocity in the near-wall region unchanged. The filter lengths vary gradually among the two regions through the use of a smoothing function $\widetilde{\Delta_i} = \Delta_i 0.5(1 \pm \tanh(z_c/(2h_\Delta))(1 - z/z_c))$ with Δ_i being the reference Gaussian filter lengths used in the streamwise and spanwise directions. In both experiments the width of the hyperbolic tangent is set to $h_\Delta = 0.2$. In the experiment θ_{out} (where the inner cycle is suppressed) Δ_i is expressed in inner units, while in the experiment

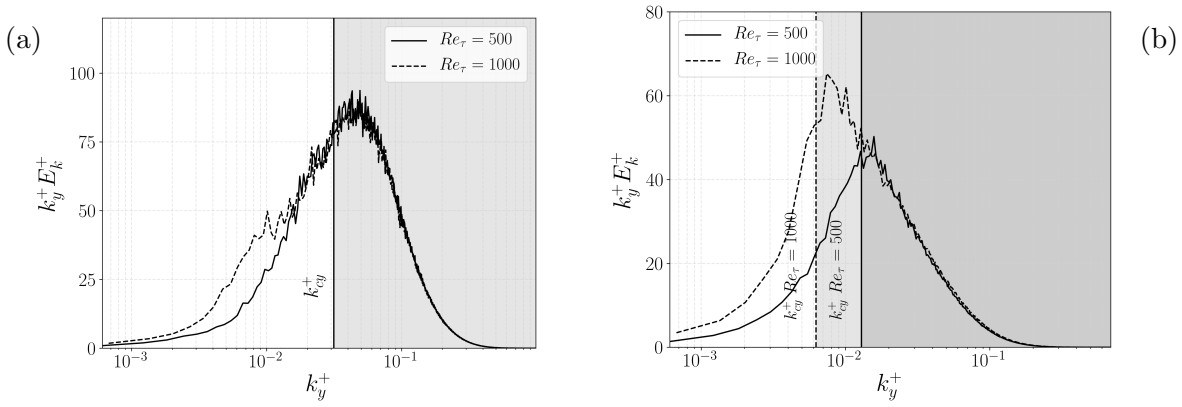

Figure A1. Premultiplied spectra of the turbulent kinetic energy E_k in the spanwise wavenumber k_y respectively (a) in the buffer layer at $z^+ = 20$ and (b) in the outer region at $z^+ = 200$. The shaded areas indicate the filtered regions of the spectra (a) in u_{out} and (b) in u_{inn}, being $k_{cy}^+ = 2\pi/\Delta_y^+$ the wavenumber corresponding to the spanwise filter length in inner units. In (b), k_{cy}^+ is reported at the initial $Re_\tau = 500$ and final $Re_\tau = 1000$.

θ_{inn} (where the outer cycle is suppressed), Δ_i is expressed in outer units. The filter lengths are chosen to remove most of the energy content in the region where they are applied. By looking at the premultiplied spectra, they have been respectively set to $\Delta_x^+ = 600$ and $\Delta_y^+ = 100$ for u_i^{out}, and $\Delta_x = 1.5\delta$ and $\Delta_y = 0.5\delta$ for u_i^{inn}. In order to ensure u_i^{inn} and u_i^{out} to be divergence free, the pressure projection method is applied to the two velocity fields after the filtering operation. The portions of the spectra filtered out in the spanwise direction to obtain u_i^{inn} and u_i^{out} are shown in shaded grey in figure A1(a) and (b), respectively measured in the buffer layer and in the outer region.

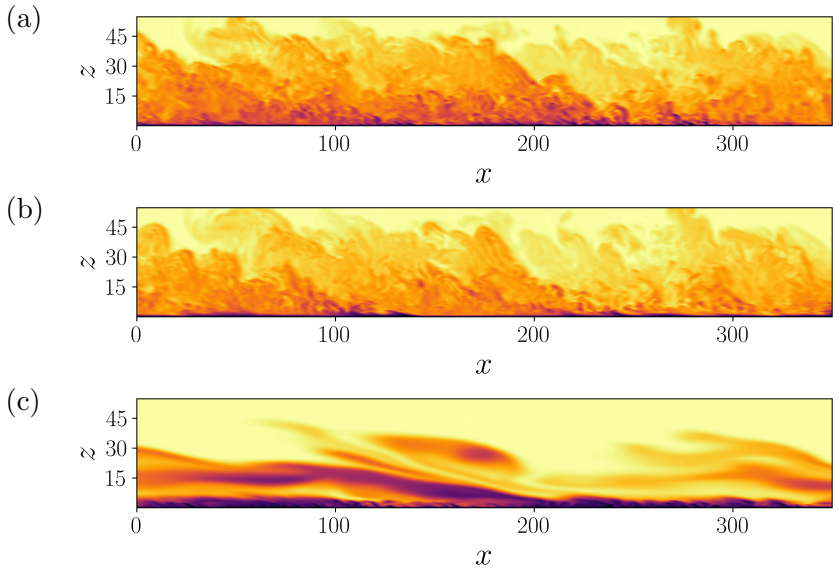

Figure A2. Sections of the scalar fields of the three experiments at the same time instant, corresponding to $Re_\tau = 1000$. Respectively (a) θ, (b) θ_{out} and (c) θ_{inn}. The reference case (a) is duplicated here in order to simplify comparisons.

We now proceed to present the results of these experiments. All the figures reported are maintained as in section 3 in order to have a clear comparison between the data. In figure 3 the instantaneous scalar contours are shown on a wall-normal section. In figure A2, the instantaneous scalar contours are shown on a wall-normal section. The scalar fields of the two experiments θ_{out} and θ_{inn} show a very different topology if compared to those obtained with the approach presented in section 3. In particular, θ_{out} looks macroscopically almost unaltered, with a rescaling toward lower scalar values. Looking closer, in the near-wall region (which is difficult to distinguish) it is possible to note substantial differences resulting from the absence of small-scale motions. On the contrary, the field θ_{inn} appears completely different with respect to the reference case due to the application of the filtering operation with large filter lengths ($\Delta_x = 1.5\delta$ and $\Delta_y = 0.5\delta$). Despite this topological difference, we will see below that the statistics of interest for this work and the main conclusions obtained in section 3 remain valid.

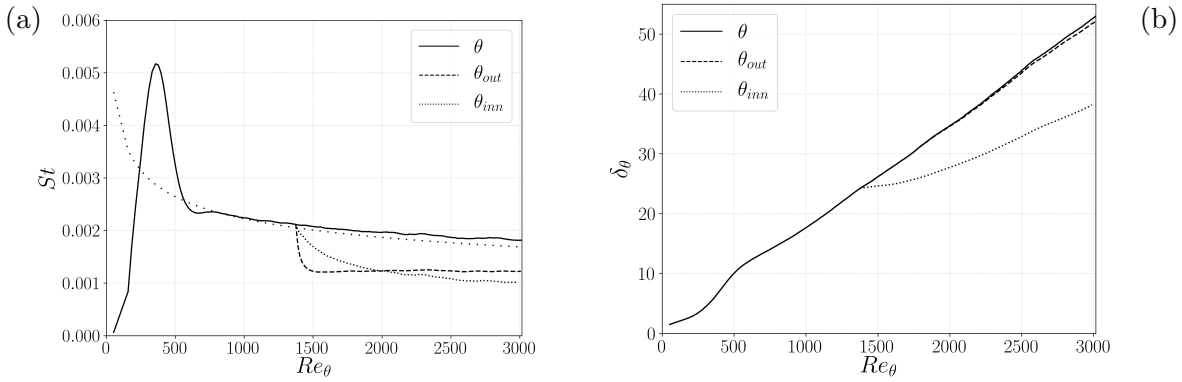

Figure A3. (a) Temporal evolution of the Stanton number and its theoretical law $St = 0.0125 Re_\theta^{-1/4}$ in loosely dotted line ($\cdots\cdots$) and (b) temporal evolution of the boundary layer thickness based on the scalar concentration δ_θ.

As shown in figures A3(a) and 4(a), the Stanton number evolutions resulting from the two approaches are qualitatively similar. Accordingly, also the pdf profiles measured in the viscous sub-layer reported in figures A4(a) and 5(a) describe a similar scenario.

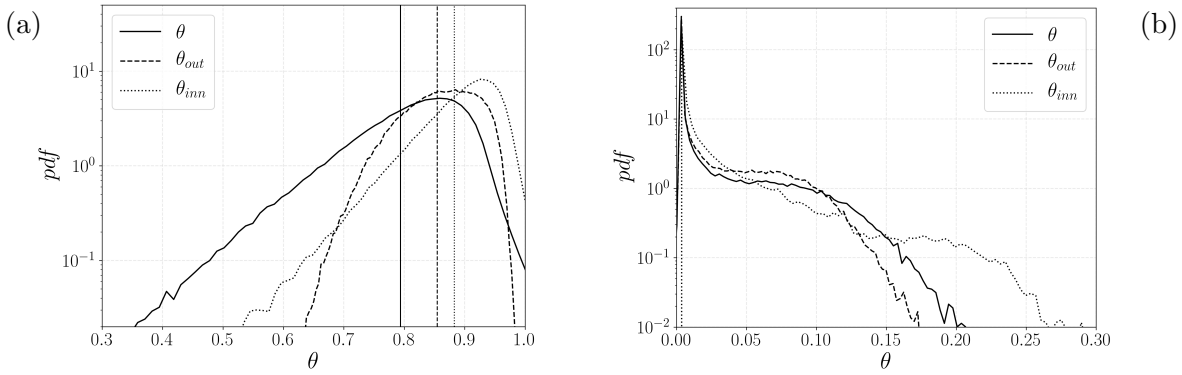

Figure A4. Probability density function of θ (a) at $z^+ = 5$ and (b) at $z = \delta_\theta$ at the final $Re_\tau = 1000$. The vertical lines in (a) indicate the respective mean values of the scalars.

A similarity can also be found in the temporal evolution of the boundary layer thickness as shown in figures A3(b) and 4(b) and in the relative pdf profiles measured at the mean scalar

interface (figures A4(b) and 5(b)). One notable difference is in the pdf distribution of θ_{inn} (dotted line). The presence of an extended right tail in the pdf of θ_{inn} in figure A4(b) is caused by the intersection between the plane located at the mean scalar interface position and the protruding bulges generated by the large anisotropic fluctuations. These bulges contain a wide range of scalar values and remain unmixed due to the absence of the small scales. The extension of this tail is more extended with respect to the first approach because of the larger filter lengths used. A minor change can also be observed in the evolution of $\delta_{\theta_{inn}}$ in figure A3(b) that is nearly identical to that of the reference δ_θ in figure A3(b). In the present approach, in fact, the velocity field in the outer region is not modified ($u_i^{inn} = u_i$) and the small difference between $\delta_{\theta_{inn}}$ and δ_θ is only the result of the lower scalar concentration flux coming from the inner cycle. This effect is comparable to a change of threshold in the definition of the mean interface position, which is therefore a very small effect.

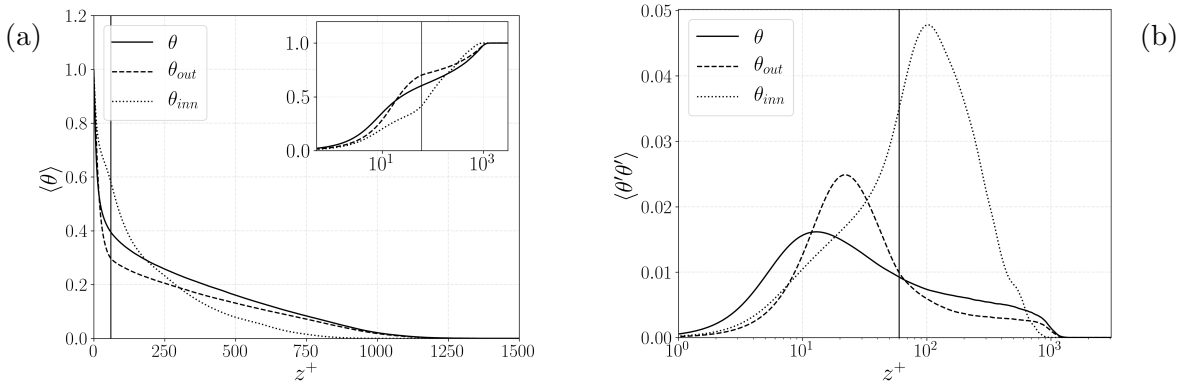

Figure A5. (a) Mean scalar profiles and (b) variances at $Re_\tau = 1000$. The solid vertical line is located at $z_c^+ = 60$.

The mean profiles reported in figure A5 show a behaviour in accordance with the one observed in figure 6, while the scalar variances describe a scenario opposite to the one observed in section 3 and in accordance with what is shown in figure A2. The highly unmixed outer region of θ_{inn} causes a peak in $\langle\theta'_{inn}\theta'_{inn}\rangle$ that have a great impact on the scalar variance fluxes, as we will see.

The mean fluxes reported in figure A6 are in good accordance with what is observed in figure 7.

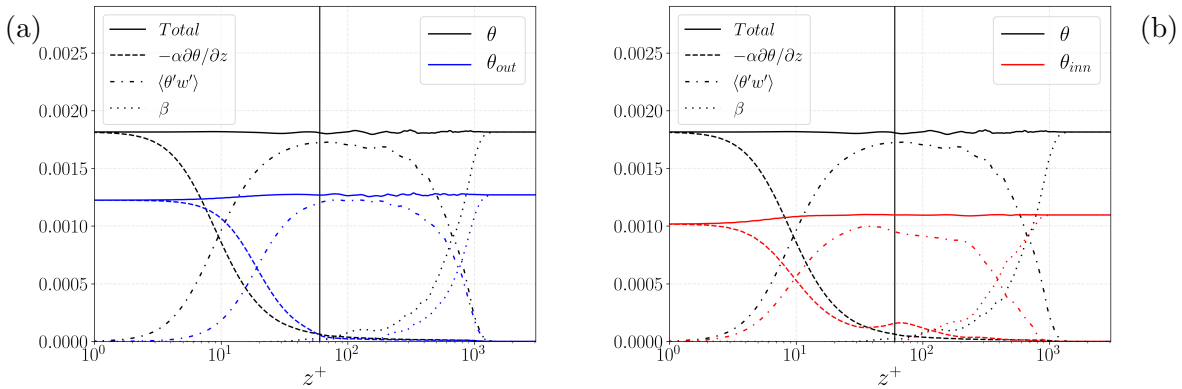

Figure A6. Mean fluxes of (a) θ_{out} and (b) θ_{inn} compared with θ at $Re_\tau = 1000$. The solid vertical line is located at $z_c^+ = 60$.

Finally, the scalar variance budgets show some macroscopic differences due to the more intrusive nature of the approach here presented. However, if we limit our analysis far enough from the region affected by the filtering operation (i.e. $z^+ \ll 60$ for θ_{inn} and $z^+ \gg 60$ for θ_{out}) we can note that the main conclusions drawn in section 3 find support in these graphs.

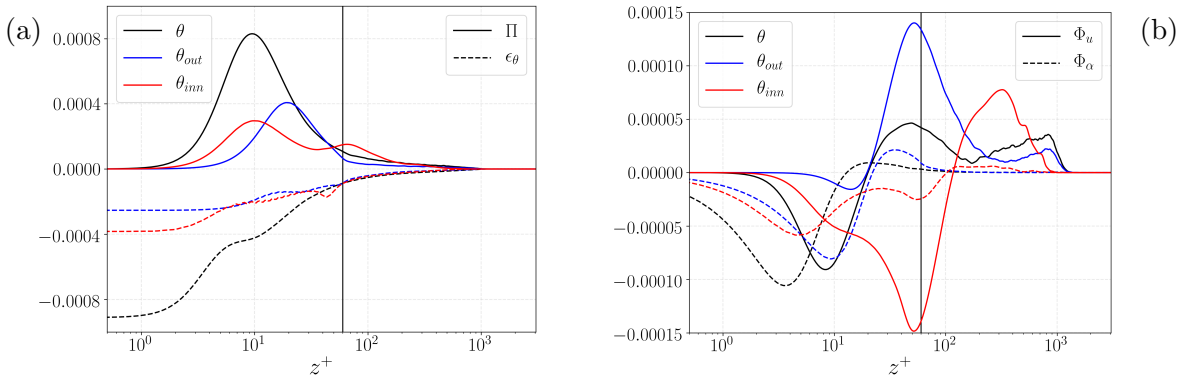

Figure A7. Scalar variance (a) production Π, dissipation ϵ_θ and (b) turbulent and diffusive fluxes Φ_u and Φ_α at $Re_\tau = 1000$. The solid vertical line is located at $z_c^+ = 60$.

To conclude, despite the topological differences shown by the corresponding scalar fields of the two presented approaches, the results obtained lead to the same conclusions in both experiments. Confirmation of this can be found in the similarities between the evolution of the integral quantities, in the mean profiles, in the turbulent fluxes of both the mean scalar concentration and its variance and the production and dissipation of the fluctuations (if confined in the regions of interest, namely the inner region for θ_{inn} and the outer region for θ_{out}).

References

[1] Smits A J, McKeon B J and Marusic I 2011 High–Reynolds number wall turbulence *Annu. Rev. Fluid Mech.* **43** 353-75
[2] Robinson S. K. 1991 Coherent motions in the turbulent boundary layer *Annu. Rev. Fluid Mech.* **23** 601–39
[3] Townsend A A 1976 *The Structure of Turbulent Shear Flows* (Cambridge: Cambridge University Press)
[4] Jiménez J and Pinelli A 1999 The autonomous cycle of near-wall turbulence *J. Fluid Mech.* **389** 335-59
[5] Mizuno Y and Jiménez J 2013 Wall turbulence without walls *J. Fluid Mech.* **723** 429-55
[6] Li Q, Schlatter P, Brandt L and Henningson D S 2009 DNS of a spatially developing turbulent boundary layer with passive scalar transport *Int. J. Heat Fluid Flow* **30** 916-29
[7] Kozul M, Chung D and Monty J 2016 Direct numerical simulation of the incompressible temporally developing turbulent boundary layer *J. Fluid Mech.* **796** 437-72
[8] Cimarelli A, Boga G, Pavan A, Costa P and Stalio E 2023 Energy cascade phenomena in temporal boundary layers *Flow Turbul. Combust.* 1-17
[9] da Silva C B, Hunt J C R, Eames I and Westerweel J 2014 Interfacial layers between regions of different turbulence intensity *Annu. Rev. Fluid Mech.* **46** 567–90
[10] Zhang X, Watanabe T and Nagata K 2023 Reynolds number dependence of the turbulent/non-turbulent interface in temporally developing turbulent boundary layers *J. Fluid Mech.* **964** A8
[11] Cimarelli A and Boga G 2021 Numerical experiments on turbulent entrainment and mixing of scalars *J. Fluid Mech.* **927** A34
[12] Costa P 2018 A FFT-based finite-difference solver for massively-parallel direct numerical simulations of turbulent flows *Comput. Math. Appl.* **76**(8) 1853-62